Proceedings of the IASS Annual Symposium 2019 – Structural Membranes 2019
Form and Force
7 – 10 October 2019, Barcelona, Spain
C. Lázaro, K.-U. Bletzinger, E. Oñate (eds.)

Efficient aeroelastic analysis of wind loads on inflatable hangars

Roberto FLORES*, Enrique ORTEGA[a]

* International Center for Numerical Methods in Engineering (CIMNE)
C. Gran Capitán s/n, 08034 Barcelona, Spain
rflores@cimne.upc.edu
[a] Serra Hunter professor at Escola Superior d'Enginyeries Industrial, Aeroespacial y Audiovisual de Terrassa (ESEIAAT), Universitat Politècnica de Catalunya, Spain

Abstract

Wind loads play a crucial role in inflatable structures. Unfortunately, design loads from safety regulations grossly overestimate the real aerodynamic forces. Thus, a more accurate estimation of wind loads is desirable. Conventional CFD approaches (e.g. LES) struggle with the complexities of the flow field (intricate geometry and massive flow separation) and require a very high computational effort. We present a cost-efficient tool for the aeroelastic analysis of inflatable hangars. It uses a staggered solution scheme with an explicit finite-element structural solver and potential flow aerodynamics. To account for large areas of separated flow typical of blunt shapes, a semi-empirical correction is applied to the inviscid solution. The streamlines of the potential solution are computed and, for each one, the separation point is predicted with Stratford's criterion. Finally, an empirical correction is applied to the inviscid pressure field. We present validation benchmarks as well as a real life application example. Over the majority of the flow field, the pressure field agrees well with high-fidelity computations, yielding similar global loads for structural sizing. This is achieved with a small fraction of the computational effort required by conventional CFD approaches

Keywords: inflatable structures, aeroelasticity, wind loads, low-fidelity methods

1. Introduction

From the point of view of analysis and design, inflatables pose special challenges, such as material characterization and structural response (both highly nonlinear), airtightness and shape stability. A typical case is the study of wind loading. The combination of low stiffness and reduced inertial mass increases the importance of the coupling between the structural and aerodynamic fields.

The first numerical tools for fluid-structure interaction (FSI) analysis of inflatables appeared in the early 90s. Air was modeled using panel methods with finite element (FE) techniques used for the structure. This methodology has proven very effective for streamlined shapes where the flow is mostly attached. Higher-fidelity FSI methods with full volume discretization incur in much higher computational cost.

In a production environment, time and computer resources are limited. Hence, methods yielding acceptable accuracy with minimal cost are necessary. Furthermore, potential users of the analysis tools have limited training in continuum mechanics and numerical analysis. To address these constraints, CIMNE & ESEIAAT co-developed a simplified simulation code, initially intended for ram-air parachutes (see https://www.cimne.com/parachutes). The solution is based on potential flow aerodynamics, explicit FE structural dynamics and staggered FSI coupling; see [1,2]. Here, we extend this methodology to simulate wind effects on inflatable structures, correcting for the special features of the flow around blunt bodies. The procedure is outlined in sections 2 and 3, and a real-life example is

presented in section 4 to illustrate the performance achieved. The most relevant conclusions are drawn in Section 5.

2. Overview of the simulation approach

We outline briefly the main characteristics of the numerical model. For further details the reader is referred to [1].

2.1. Structural modeling

The structural solver is based on a large-displacement dynamic FE formulation. A wrinkling model is used to account for the lack of compression stiffness in cables and membranes. When computing stresses, small tensile strains are assumed, but arbitrarily large compressive strains are allowed to account for wrinkling. The equations are advanced in time with an explicit second-order scheme. A numerical dissipation model with Rayleigh damping and bulk viscosity is used to control local high-frequency modes that are not well resolved by the staggered coupling adopted. This approach is simple and inexpensive, but care must be taken to avoid contamination of the solution with spurious viscous forces. Guidelines for tuning the damping parameters are given in [1,3].

The solver models cables, membranes and 3D solids using 2-node linear, 3-node triangular and 4-node tetrahedral elements, respectively. Line elements are used for simulating the anchoring and stabilization cables, fabric seams and reinforcement tapes. The solid tetrahedral elements model ballasts and any other suitable components. If the deformations of the parts discretized with volume elements are negligible compared with the rest of the structure, groups of solid elements can be lumped into rigid bodies to reduce the model complexity.

Different types of kinematic constraints and analytical contact with pre-defined surfaces are available to accommodate the different support conditions found in real life. In addition, it is possible to prescribe time-varying tube pressurization (for inflation and deflation analyses) and several types of distributed loads (e.g. fixed-direction and follower) to simulate wind and snow actions.

2.2. Aerodynamic modeling

The flow is solved with a low-order unsteady panel method using doublets and sources. Constant strength panels lower complexity and computational cost. Also, the discretization is simplified because exact matching between panels is not required. Wake rollup is included via time-steeping technique. Unsteady added mass effects are also simulated, and drag forces on cables and simple bodies are accounted for by means of empirical coefficients. For this work, the unsteady capabilities of the solver have not been used, only steady-state results are presented.

The atmospheric boundary layer is model with an exponential wind profile according to the Eurocode 1 standards (EN 1991-1-4: wind actions, see [4]). In the context of potential flow, boundary layers can be approximated as a uniform far-field inflow velocity plus a local velocity correction at the surface of the structure that depends on the distance to the ground. Hence, the irrotationality of the velocity field is preserved.

Although simple and effective, the inviscid solution approach is only suitable for solving attached flows. The next section describes the strategy to include the effect of separation.

3. Flow detachment correction

In flows with extensive and well-defined areas of detached flow, experiments show that the pressure field over the areas where the boundary layer remains attached does not differ much from an inviscid solution. The main differences appear in the separated area because the pressure recovery downstream of the separation point stops and the time-average pressure in the near-wake becomes almost constant. Since in blunt body problems pressure is the main contribution to the aerodynamic forces, these

observations suggests a simple correction of the inviscid solution. At the beginning of each time step the inviscid solution is used to predict the separation points. Next, the pressure downstream of the detachment area is corrected by keeping the value constant. Finally, the corrected pressure field is transferred to the FE solver to calculate the structural response.

There are numerous methods in the literature that combine approximate boundary layer solutions and empirical data to estimate the point of separation [5,6]. In this work, Stratford's method [7] is used due to its efficiency and acceptable accuracy. As the criterion was developed for 2D and axisymmetric problems [8], it is applied along the flow streamlines. The method can be applied to fully turbulent and laminar-turbulent flows. It yields an averaged (quasi-steady) pressure field accounting for separation. The main implementation details of the procedure are described next.

3.1. Streamline calculation

The first step for the correction of the inviscid solution is to recover the flow streamlines. To this end, the inviscid solver computes the velocity and pressure at the center of each panel in the solid surface. The velocity field is normalized and a linked-list is constructed to identify, for each surface panel *i*, its corresponding downstream panel *i+1*. The search is performed over the nearest panels, skipping those already tagged. Panels where flow reversal takes place are also marked at this stage.

Using the linked-list, the streamlines are constructed starting from the forward stagnation areas until there are no remaining downstream panels or flow reversal occurs (which indicates the rear stagnation area has been reached).

3.2. Prediction of separation points

Stratford's model predicts the detachment of incompressible high-Reynolds flows using a two-layer approach. Closer to the surface, in the inner part of the boundary layer, the pressure forces are balanced by the gradient of the viscous stresses. In the outer layer the flow is assumed nearly inviscid, and the pressure forces are balanced by inertial forces through variation of dynamic pressure. The model formulation and validation examples can be found in [7]. In the present work, the guidelines given in [5, 9] are followed with the objective to emphasize the implementation aspects.

It is assumed that the points $\boldsymbol{x}_i$ along each streamline can be connected by straight lines, so the distance between them is approximately the Euclidean distance between the centers of the panels. In streamline coordinates the first point (stagnation point) is located at the origin $x_0=0$ and the position of the downstream points $i=1,2,\ldots n$ is calculated as $x_i = x_{i-1} + \left\| \mathbf{x}_i - \mathbf{x}_{i-1} \right\|$. For each streamline the position of the point of maximum velocity x_m is determined. When applicable, the transition location $x_t < x_m$ at which the flow switches to fully turbulent is also stored. This can be prescribed (user-input) or calculated with a suitable transition criterion. The downstream position of the separation point x_s is the solution sought.

The characteristic points are shown in figure 1, where the position is plotted against $\left(1-\bar{C}_p\right)$. The parameter $\bar{C}_p$ is the pressure coefficient at a point referred to the conditions at the point of maximum velocity x_m

$$\bar{C}_p = \frac{p - p_m}{q_m} = 1 - \frac{q}{q_m} \tag{1}$$

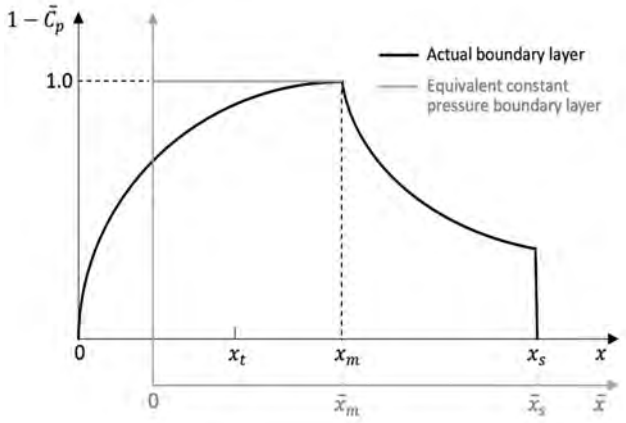

Figure 1: Actual and equivalent pressure distributions along a streamline and characteristics points [9]

An additional coordinate system $\bar{x}$ is depicted in figure 1, intended for general cases including boundary layer transition and favorable pressure gradients (the original criterion only applies to fully turbulent boundary layers with adverse pressure gradients). To treat these cases, Stratford made the assumption that at $x=x_m$ the actual velocity profile can be assimilated to that of a flat-plate turbulent boundary layer whose leading edge is located at $\bar{x}_0 = x_m - \bar{x}_m$. Hence, $\bar{x}_m$ is the length of an equivalent constant pressure region over which a turbulent boundary layer would develop the same momentum thickness θ as the actual laminar-turbulent boundary layer over the distance x_m. The velocity profile at this point is approximated by a power-law $u/U_m = (y/\delta)^{1/n}$. With these considerations, Stratford's criterion for the location of the separation point can be expressed as [9]

$$\left(2\bar{C}_p\right)_s^{(n-2)/4}\left(\bar{x}\frac{d\bar{C}_p}{dx}\right)_s^{1/2} = N\beta\left(10^{-6}\overline{\mathrm{Re}}\right)^{1/10} \tag{2}$$

where subscript *s* indicates values measured at the separation point, $\overline{\mathrm{Re}} = U_m\bar{x}_m/\nu$ and

$$N = 11.36\frac{(n-2)^{(n-2)/4}}{(n+1)^{(n+1)/4}(n+2)^{1/2}} \tag{3}$$

In equation (1) the empirical parameter β depends on the shape of the boundary layer near separation. Values of β=0.66 and 0.73 are suggested in [39] depending on the sign of $d^2\bar{C}_p/dx^2$. Following [9] we adopted a value n=6 for the boundary layer shape parameter. Using these values, the separation criterion becomes

$$\frac{\left(2\bar{C}_p\right)_s\left(\bar{x}\frac{d\bar{C}_p}{dx}\right)_s^{1/2}}{\left(10^{-6}\overline{\mathrm{Re}}\right)^{1/10}} = S(x) = \begin{cases} 0.35 & \text{for} \quad d^2\bar{C}_p/dx^2 < 0 \\ 0.39 & \text{for} \quad d^2\bar{C}_p/dx^2 \geq 0 \end{cases} \tag{4}$$

Eq. (3) is evaluated at each point x_i along the streamline starting from the x_0 and separation is predicted where S(x) reaches the indicated values.

The length of the equivalent boundary layer $\bar{x}_m$ needed to compute $\overline{\mathrm{Re}}$ in Eq. (3) is obtained from [9]

$$\overline{x}_m = 38.2\left(\frac{\upsilon}{U_t x_t}\right)^{3/8}\left[\int_0^{x_t}\left(\frac{U}{U_t}\right)^5 dx\right]^{5/8} + \int_{x_t}^{x_m}\left(\frac{U}{U_m}\right)^3 dx \tag{5}$$

where the transition location x_t can estimated with Michel's method [10]. It is based on a correlation for the local momentum thickness given by

$$\mathrm{Re}_{\theta,t} = \frac{U(x)\theta(x)}{\upsilon} \approx 2.9\,\mathrm{Re}_{x,t}^{0.4} \tag{6}$$

where the subscript t denotes values measured at the transition point. We compute the momentum thickness $\theta(x)$ using Thwaite's method [9]

$$\theta(x) = \frac{0.45\upsilon}{U_m^6}\int_0^x U^5(x)dx \tag{7}$$

Note that the separation distance $\overline{x}_s$ predicted by Eq. (4) must be corrected to take into account the actual boundary layer length. Thus, the real separation point is $x_s = x_m + (\overline{x}_s - \overline{x}_m)$.

4. Application example: two-way coupled solution of an inflatable hangar with wind loads

We study a Buildair's H20 inflatable hangar [11] subject to lateral wind (β=90º. The hangar's internal width and height are 20.5 m and 10.25 m, respectively. It is built using 11 tubes (3.5 m in diameter each) that make up a total length of 31.2 m. The discrete model (figure 2) uses 21374 quadrilaterals elements for the fabric (split internally into triangles by the structural solver) and 8014 line elements for the anchoring cables, seams and reinforcements. A symmetry plane is included to model the ground surface. For the aerodynamic simulation, an atmospheric wind profile with basic velocity 90 km/h is prescribed according to the EN 1991-1-4 standards. The Reynolds number based on the outer hangar's diameter is about $47 \cdot 10^6$, high enough that fully turbulent flow can be assumed. An inflation pressure of 3000 Pa is applied to the tubes. The fabric is a pvc-coated polyester with Young's modulus of 0.38 GPa, 0.5 mm thickness and surface density of 590 g/m^2. The reinforcements have a Young's modulus of 2.5 GPa, 2 mm thickness, 50 mm width and linear density 85 g/m.

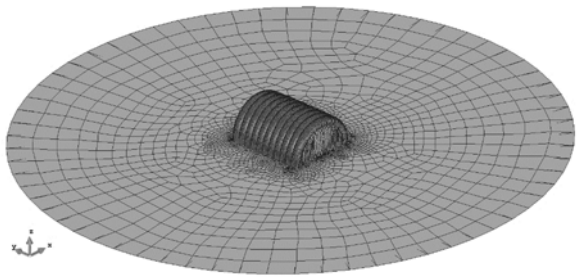

Figure 2: Buildair H20 hangar discrete model and symmetry plane

The objective of the analysis is to determine the steady-state deformations and stresses caused by the wind loads. The steady two-way coupled solution requires 26 s of physical simulation time. This takes about 1 hour CPU-time running in a desktop computer with an Intel Core2 Quad Processor Q9550 @ 2.83 GHz (using 4 cores). The predicted flow separation area and the corrected pressure field are shown in figure 3. The solution captures the main features of the flow around the hangar satisfactorily, although small higher-pressure areas appear at the rear of the hangar. These are not completely eliminated the detachment correction, probably due to a stagnant flow that disrupts the streamlines

over this area. However, since only a small surface is affected, the impact on the overall loads is negligible.

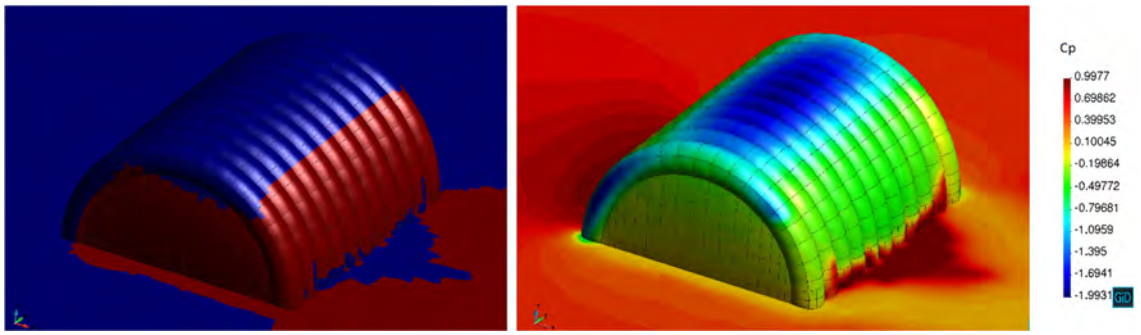

Figure 3: H20 under lateral wind. Views of the detached flow area (left, colored in red) and the corrected Cp field (right) obtained for the steady-state problem solution

The steady pressure distribution calculated along the central tube (#6) is compared in Figure 4 with higher-fidelity CFD results and standard design loads from EN 1991-1-4. The CFD results have been computed with the incompressible Navier-Stokes solver Tdyn [12], using the Spalart-Allmaras turbulence model and law-of-the-wall boundary conditions. Although building regulations consider neither the exact shape of the hangar nor the aeroelastic redistribution of loads, these estimations are often used in preliminary design when specific results are not available. Hence, it is useful to have a measure of the differences expected in such cases. There is a good agreement between our coupled solution and the CFD calculation for the windward side, although the suction peak obtained is higher (about 20%) and somewhat displace3d downstream with respect to the high-fidelity result. The detached flow area is well captured by our solution and the overall comparison is satisfactory. Regarding the loads computed from the EN 1991-1-4 standard, these underestimate the maximum and minimum pressures compared to our results and the CFD solution.

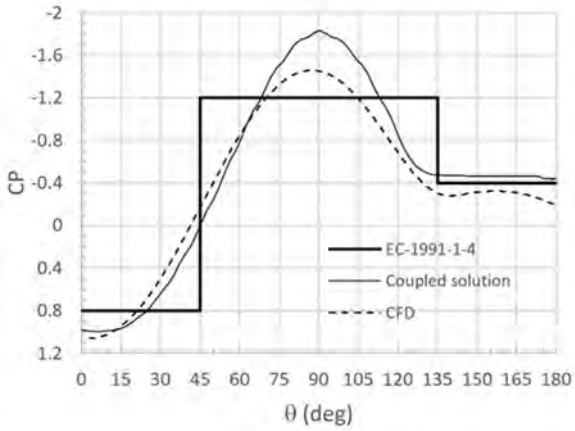

Figure 4: Cp distributions calculated along the central tube of the hangar H20 for a lateral wind condition. Comparison of coupled solution with CFD and standard design loads

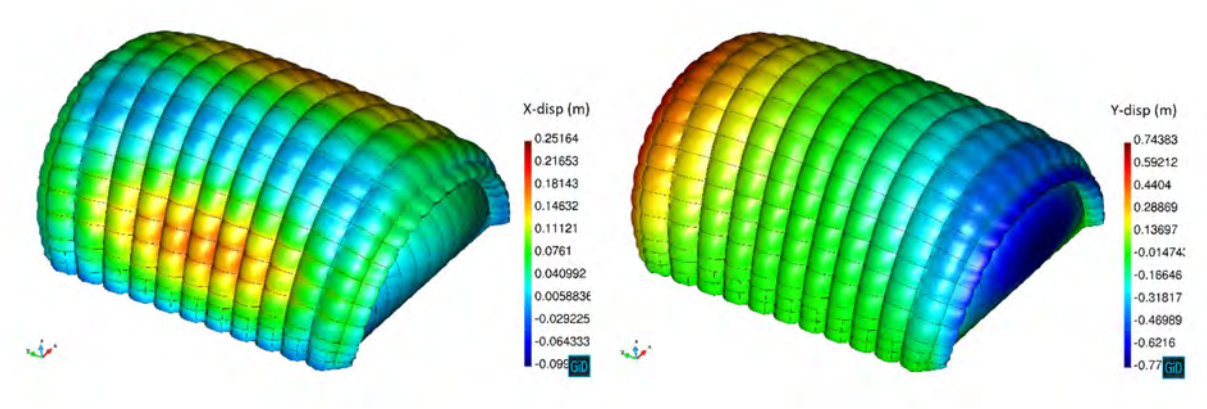

Figure 5: H20 transverse (left) and longitudinal (right) displacements (displacement magnification x5)

Figure 5 shows the computed horizontal displacements. The maximum lateral and longitudinal displacements are 0.25 and 0.75 meters, respectively. As shown in figure 6 (left) the maximum vertical displacement of the roof is 0.55 m. The figure also displays the reaction forces at the anchor points (right). Finally, the fabric principal stresses are plotted in Figure 7.

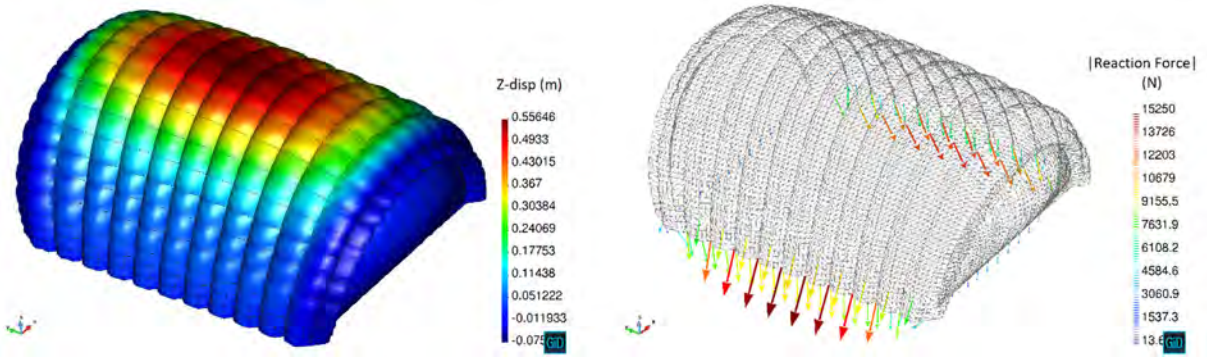

Figure 6: H20 vertical displacements and anchoring reaction forces (displacement magnification x5)

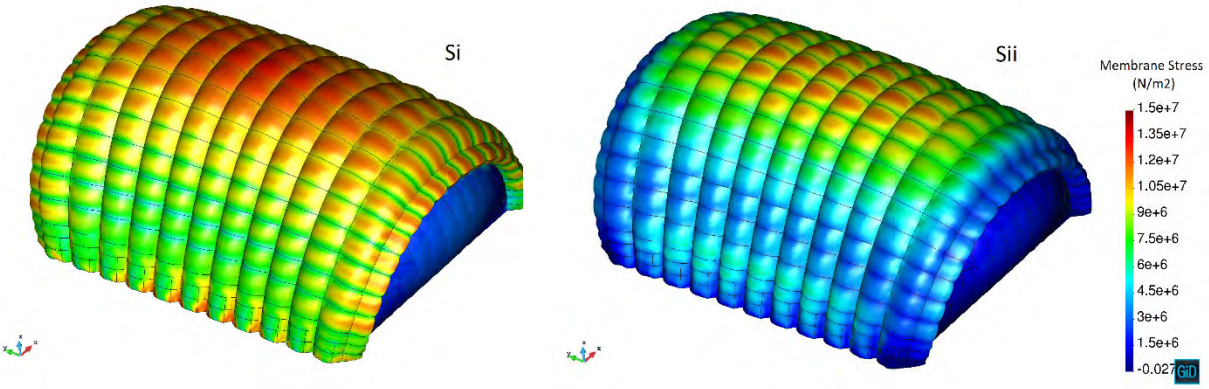

Figure 7: H20 fabric principal stresses S1 and S2 (displacement magnification x5).

4. Conclusions

We presented a cost-effective approach to aeroelastic analysis of inflatable structures under wind loading. It combines explicit finite-element structural dynamics and enhanced potential flow aerodynamics. The inviscid flow field is modified to take into account the massive flow separation

typical of bluff shapes. The potential solution is used to predict the detached flow areas (using Stratford's method) and the pressure field is corrected accordingly.

Overall, the results obtained indicate that the enhanced aerodynamic model can estimate wind loads on inflatable bluff structures with reasonable accuracy, at a small fraction of cost of high-fidelity CFD approaches. It can prove especially useful in the design of structures with unconventional characteristics, where standard design practices become unreliable.

Acknowledgements

The authors wish to thank BuildAir Inflatable Structures Solutions S. A. (www.buildair.com) for providing analysis models, test data and many other useful inputs during the development of this work.

References

[1] R. Flores, E. Ortega and E. Oñate, "Simple and efficient numerical tools for the analysis of parachutes," *Engineering Computations*, vol. 31, issue 5, pp. 957-985, 2014.

[2] E. Ortega, R. Flores and J. Pons-Prats, "Ram-Air Parachute Simulation with Panel Methods and Staggered Coupling," *Journal of Aircraft*, vol. 54, issue 2, pp. 807-814, 2017.

[3] D. de la Torre, E. Ortega and R. Flores, *PARACHUTES. A computer program for calculating ram-air parachutes. User's manual*. CIMNE publications, 2015.

[4] N. Cook, *Designers' Guide to EN 1991-1-4 Eurocode 1: Actions on structures, general actions part 1-4. Wind actions*. Thomas Telford Publishing, 2007.

[5] T. Cebeci, G.J. Mosinskis and A.M.O. Smith, *Calculation of Viscous Drag and Turbulent Boundary-Layer Separation on Two-Dimensional and Axisymetric Bodies in Incompressible Flows*. Report MDC-J0973-01, Douglas Aircraft Co, 1970.

[6] P.M. Gerhart and L.J. Bober, *Comparison of several methods for predicting separation in a compressible turbulent boundary layer*. NASA TM X-3102, 1974.

[7] B.S. Stratford, "The prediction of separation of the turbulent boundary layer," *Journal of Fluid Mechanics*, vol. 5, issue 1, pp. 1-16, 1959.

[8] A.M.O. Smith, "Stratford's turbulent separation criterion for axially-symmetric flows," *Journal of Applied Mathematics and Physics (ZAMP)*, vol. 28, issue 5, pp. 929-939, 1977.

[9] A.M. Kuethe, A.M. and C.Y. Chow, *Foundations of Aerodynamics. Bases of Aerodynamics Design*. John Wiley & Sons, 1997.

[10] R. Michel, *Etude de la Transition sur les Profiles d'Aile; Etablissement d'un Critére de Determination de Point de Transition et Calcul de la Trainee de Profile Incompressible*. ONERA Report, 1951.

[11] Buidair's outstanding projects - Hangars - H20 Poland. Available online, last checked May 2019. http://www.buildair.com/projects-delivered/hangers-h20-poland/

[12] E. Oñate, F. Flores and J. Marcipar, "Membrane Structures Formed by Low Pressure Inflatable Tubes. New Analysis Methods and Recent Constructions." in *Textile Composites and Inflatable Structures II, Stuttgart, Germany, October 2-4, 2005*, Springer, 2008, pp. 163-196.